Journal of Power Sources 211 (2012) 108–118

Contents lists available at SciVerse ScienceDirect

Journal of Power Sources

journal homepage: www.elsevier.com/locate/jpowsour

Fabrication and characterization of Li–Mn–Ni–O sputtered thin film high voltage cathodes for Li-ion batteries

Loïc Baggetto*, Raymond R. Unocic, Nancy J. Dudney, Gabriel M. Veith

Materials Science and Technology Division, Oak Ridge National Laboratory, 1 Bethel Valley Road, Oak Ridge, Tennessee 37831, USA

ARTICLE INFO

Article history:
Received 20 February 2012
Received in revised form
15 March 2012
Accepted 17 March 2012
Available online 10 April 2012

Keywords:
High voltage spinel cathodes
Magnetron sputtering
Thin films
Layered-spinel composite structure
Coatings

ABSTRACT

Li-rich and stoichiometric $Li_1Mn_{1.5}Ni_{0.5}O_4$ (LMNO) cathode films have been successfully prepared by magnetron sputtering. Sputtering from a Li stoichiometric target yields Li-rich films composed of spinel, layered and monoclinic phases. Films obtained from a Li deficient target are mostly made of a spinel phase and little layered material. The resulting cathode thin films have good capacity retention and very high rate capability. The reaction mechanism has been investigated by XRD and HRTEM and evidences the reversible formation of a spinel phase, as is generally found for the powder samples. The film geometry enables us to understand the effect of coatings (ZnO or LiPON). Coating high voltage cathodes reduces the coulombic losses, but at the price of rate performance. Nonetheless, these coated sputtered electrode thin films offer a higher rate capability than other LMNO thin films obtained by other physical vapor deposition techniques.

1. Introduction

Since their introduction in 1991, rechargeable lithium-ion batteries have enabled a profound revolution in our daily lives. The current widespread use of portable electronic devices such as smart phones and laptop computers is an obvious example [1]. Nowadays, the current research efforts are intensely focusing on the application of Li-ion batteries for automotive applications. In order to achieve the performance requirements necessary for automotive applications, cathodes with larger storage capacities and higher operating voltages, along with electrolytes which have a larger stability window are necessary to produce more durable and high power batteries.

High voltage spinel cathodes have attracted a lot of attention as alternatives to conventional layered cathodes [2]. $LiMn_{1.5}Ni_{0.5}O_4$ (LMNO) is of particular interest as the material has a reaction voltage near 4.7 V vs. Li and a theoretical gravimetric capacity of about 147 mAh g^{-1} [2]. The operation at high voltages stems from the oxidation of Ni^{2+}; the Mn^{4+} cations are electrochemical spectators but provide structural stability [3,4]. Moreover, LMNO cathodes possess very high rate capability due to the 3D diffusion pathways for Li ions inside the spinel structure [5–7].

Despite these advantages, side reactions between the cathode and electrolyte solution remain an issue for practical applications [8–10]. These deleterious effects found for high voltage cathodes, especially at high temperatures, result from undesired reactions with the electrolyte solution. Indeed, it is known that the capacity retention at elevated operating temperatures is somewhat poor due to Mn leaching or electrolyte decomposition [8]. Electrolyte contaminants and cycling by-products, such as HF, can damage the electrode surface by acidic dissolution [9]. Moreover, complete LMNO cells often suffer from internal discharge [10]. It is also generally believed that the decomposition of the electrolyte can lead to the formation of a passivation layer known as Cathode Electrolyte Interface (CEI), which hinders the interparticle conduction of charges that in turn increases the internal impedance [11].

Several groups have demonstrated that coating high voltage cathodes with an insulating metal oxide or phosphate (ZnO, ZrO_2, $AlPO_4$, Li_3PO_4, et cetera) reduces capacity losses and extends the electrode cycle life [11–20]. Although the coating is claimed to prevent deleterious (electro)chemical reactions between the electrolyte and cathode materials, scavenge undesirable species present in the electrolyte that may be created during cycling (e.g. HF), or suppress the dissolution of transition metals such as Mn, its precise role has not been thoroughly investigated [11–20].

One of the difficulties in understanding these interfaces is the complex surface chemistry of composite electrodes, which

* Corresponding author. Tel./fax: +1 8652416126.
E-mail address: baggettol@ornl.gov (L. Baggetto).

0378-7753/$ – see front matter © 2012 Elsevier B.V. All rights reserved.
doi:10.1016/j.jpowsour.2012.03.076

generally consist of the active material particles coated by carbon conductive particles, embedded in a polymer binder matrix [11–20]. Thin film electrodes are an ideal platform to understand how the coating mitigates capacity losses. Thin films have a well-defined geometric surface area and the amount of material can be accurately controlled. This is very useful for studying the surface charge transfer kinetics or the bulk diffusion across particles of known dimensions. Moreover, no binder or additives are used, which facilitates the study of properties intrinsic to the cathode material. Furthermore, the preparation of uniform coatings with controlled thicknesses on the cathode surface is much easier to achieve than coating powder particles of various, and often inhomogeneous, structures and sizes. To date, there has been little work on thin films of the spinel LMNO. Studies on uncoated LMNO thin films prepared by electrostatic spray deposition (ESD) [21,22], pulsed laser deposition (PLD) [23,24] or spin coating [25] were reported, with emphasis toward bulk and surface kinetics which proved to be very good.

Sputtering is a versatile technique for producing a wide chemistry range of cathode thin films for Li-ion batteries [26,27]. For instance, the stoichiometry of $Li_xMn_{2-}O_4$ (LMO) spinel thin films can be varied simply by adjusting some crucial deposition parameters (gas and reactor pressure), and results in the fabrication of Li-rich LMO films [26,27]. The excess of Li can be advantageous as it can be used, for instance, in a thin film battery comprising a conversion anode. This type of anode is attractive as it can provide a better cycle life at the expense of some irreversible capacity consumed during the first cycle [27].

Here we demonstrate that the resulting structure and properties of sputter deposited LMNO cathodes can be tuned by varying the Li content in the target material. This control yields thin film cathode material structures analogous to integrated layered-spinel composite electrodes [28,29]. Next, we present the characterization of the starting materials by means of Scanning Electron Microscopy (SEM), X-ray Photoelectron Spectroscopy (XPS), X-Ray Diffraction (XRD) and High Resolution Transmission Electron Microscopy (HRTEM). Moreover, we tracked the changes occurring in the bulk of the electrode using *ex situ* XRD and HRTEM. Solid-state electrolytes such as Li_3PO_4 and LiPON are electronic insulators but ionic conductors which are well-known for drastically improving the capacity retention of anode [30] and cathode thin films [31]. These materials are also essential in the fabrication of Li-ion thin film microbatteries [26,27]. Another coating material of interest is ZnO, a semi-conductor which was reported be very effective for improving the capacity retention of LMNO high voltage spinel cathodes [12]. Thus, the role of these coatings on the electrode performance was investigated using electrochemical rate cycling and Electrochemical Impedance Spectroscopy (EIS).

2. Experimental

2.1. Targets and films preparation

LMNO thin films were deposited onto Pt-coated Al_2O_3 substrates (Coorstek or Valley Design) by means of magnetron sputtering using homemade targets. The starting LMNO powder used for making the targets was prepared using a two-step solid-state reaction, as described by Hagh et al. [32]. In brief, MnO_2, NiO or $Ni(OH)_2$ (Alfa Aesar) were mixed with a Mn/Ni molar ratio of 3. The mixture was ball-milled for 1 h, recovered, pressed and fired at 900 °C for 5 h to form a $Ni_{2/3}Mn_2O_4$ spinel phase. Next, the pellet was ground and mixed with the appropriate amount of Li_2CO_3 (Mallinckrodt). Three nominal compositions were investigated, i.e. $Li_1Mn_{1.5}Ni_{0.5}O_4$, $Li_{0.75}Mn_{1.5}Ni_{0.5}O_4$ and $Li_{0.5}Mn_{1.5}Ni_{0.5}O_4$, respectively denoted Li_1MNO, $Li_{3/4}$MNO and $Li_{1/2}$MNO. The mixing was followed by another ball-milling and pressing sequence, and a final firing. This firing was achieved at 1000 °C for 15 h followed by a slow cooling of 0.5 °C min^{-1} to 700 °C maintained 40 h, and a final cooling to room temperature at 0.5 °C min^{-1}.

For the film deposition, the target-substrate distance was 5 cm. The other sputtering deposition parameters are listed in Table 1. For the structural characterization, thick layers were prepared (1.5–2 μm and annealed in air at 750 °C for 2 h) whereas thinner films (0.4 μm and annealed in air at 700 °C for 1 h) were employed for the electrochemical measurements. In all cases, 10 °C min^{-1} heating and cooling ramps were applied. ZnO and LiPON coating thin films were prepared by reactive sputtering using the conditions provided in Table 1.

2.2. Thin film characterization

SEM and Energy Dispersive X-ray analysis (EDX) were acquired using a JEOL JSM-6500F Field Emission SEM equipped with an EDAX detector. XRD scans were acquired with a Scintag Pad V diffractometer equipped with Cu K_α source and Ni filter scanned from 15 to 70° 2θ over 3.5–9 h; longer scans were used to increase the signal to noise ratio. Surface chemistry was estimated using a PHI 3056 XPS spectrometer with an Mg source in a 2×10^{-8} Torr vacuum chamber. High resolution scans were taken with 5.85 eV pass energy, 0.05 eV energy step, and 100–300 repeats to improve the signal to noise ratio. Survey scans were measured at 93.9 eV pass energy, 0.5 eV energy step and 30 repeats. The binding energies were shifted by setting the aliphatic carbon signal to 284.8 eV. The spectra were deconvoluted using Gaussian–Lorentzian functions.

In order to minimize air exposure for TEM characterization, the electrodes were extracted from the electrochemical cells and rinsed with DMC (Sigma Aldrich) inside an Ar-filled glovebox, then transferred with minimum air exposure (about 1 min) to a vacuum chamber to be sputter coated with a protective layer of about 30 nm Pt. HRTEM imaging and selected area electron diffraction (SAED) was performed using a FEI Titan S 80–300 S/TEM instrument. FIB-prepared TEM cross-sections were fabricated with a Hitachi NB5000 FIB-SEM instrument. Final thinning and removal of FIB-milling redeposition products and surface contaminants was performed using a Fischione instruments model 1040 nanomill. Electron energy loss spectroscopy (EELS) was used to determine valence state changes from Mn and Ni L_3/L_2 white lines intensity ratio method and were acquired using a Gatan Quantum GIF spectrometer.

Electrochemical measurements were conducted with either 2-electrode coin cells (2032 hardware) or Swagelok cells prepared inside an Ar-filled glovebox. The cells comprised pure Li as counter electrode, two pieces of Celgard 2500 separator and 1.2 M $LiPF_6$ in ethylene carbonate/dimethyl carbonate (EC/DMC 3:7 per volume) mixture as electrolyte (Purolyte®, Novolyte). Standard electrochemical tests were done using coin cells while swagelock cells were used for performing *ex situ* XRD and TEM on the recovered electrodes. Galvanostatic measurements were performed on a Maccor 4000 series. 1C-rate, which is equivalent to the current

Table 1
Deposition conditions for magnetron sputtered thin films.

Material	Target material	Sputtering mode	Pressure (mTorr)	Gas	Gas flow (sccm)	Power (W)
Pt	Pt (99.999%)	DC	20	Ar	20	20
LMNO	Li_xMNO	RF	5	Ar	57	80
ZnO	Zn (99.995%)	DC	20	Ar/O_2	20/10	20
LiPON	Li_3PO_4	RF	20	N_2	20	60

required to discharge the full electrode capacity in 1 h, is typically equal to 20 $\mu A\,cm^{-2}$ for the films used in the electrochemical experiments. Rate measurements were performed using a 1C-rate charge current and discharge currents of 1, 2, 3, 5, 7, 10, 20, 30, 50, 70 and 100 C-rate. EIS was conducted on a Solartron 1470E/1455A using 10 mV amplitude potential signal from 1 Mhz to 0.1 Hz.

3. Results and discussion

Surface morphology and particle size of the post-annealed films were investigated by SEM, Fig. 1. No significant differences were observed between films grown from targets of composition Li_1MNO and $Li_{3/4}MNO$. The films are polycrystalline and composed of fine grains (typically 50–150 nm, as confirmed by TEM) which do not vary substantially in size as a function of annealing temperature and time. EDX analysis reveals Mn/Ni ratios between 2.5 and 2.7 (c.f. Table 2) as has also been measured for the starting target materials, in close agreement with the expected value of 3. The ratio does not change as a function of annealing, which indicates that Mn and Ni are not lost during the final annealing. The O and Li concentrations could not be determined using EDX. For the former, Mn L-edge partly overlaps with O K-edge, which makes the quantification of O rather unreliable, whereas Li is too light to be detected by this technique.

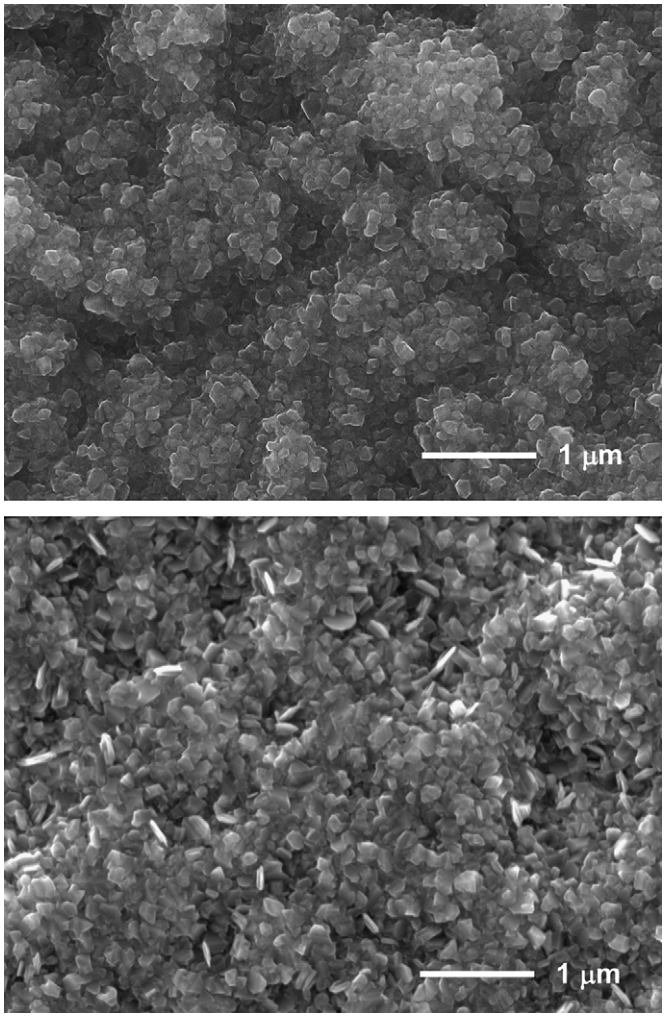

Fig. 1. Representative SEM photographs of LMNO thin films post-annealed in air. The upper image is for a film sputtered from the Li_1MNO target and annealed at 700 °C for 1 h whereas the lower image is for a film sputtered from the $Li_{3/4}MNO$ target and annealed at 750 °C for 2 h.

Table 2
Mn, Ni, C and O atomic concentrations obtained from XPS survey scan on thin films. For the quantification of Ni and Mn concentrations, the 2*p*3/2 peaks were used. The Mn/Ni ratios obtained from EDX on thin films are also reported.

Target material	Mn (at%)	Ni (at%)	C (at%)	O (at%)	Mn/Ni (XPS)	Mn/Ni (EDX)
Li_1MNO	14.7	4.5	27.2	53.6	3.27	2.70
$Li_{3/4}MNO$	14.2	3.8	32.9	49.1	3.74	2.53
$Li_{1/2}MNO$	15	3.5	37.6	43.9	4.28	2.60

The structure of post-annealed thin films determined by XRD is presented in Fig. 2. In order to ease the identification of the diffraction peaks related to the spinel phase, a reference pattern for the powder material is inserted (upper curve). Apart from the diffraction resulting from the Al_2O_3 substrate and Pt current collector (vertical dashed and full bars, respectively), several other diffraction lines are measured from the films. For the samples obtained by sputtering Li_1MNO and $Li_{3/4}MNO$ targets, the main reflections are assigned to LMNO spinel. A few weaker lines are visible on the right of the diffraction peaks related to the spinel and may be attributed to a layered material (labeled L). Moreover, very weak peaks around 21–23° are also observed (labeled M), especially for the sample sputtered from Li_1MNO target. These additional peaks might be attributed to a monoclinic Li_2MnO_3 (M) phase. The results seem to indicate the coexistence of monoclinic and layered domains with the expected LMNO spinel structure, consistent with the formation of a layered-spinel composite electrode, i.e. a composition $x[LiMn_{1.5}Ni_{0.5}O_4] + (1-x)$ $[Li_2MnO_3 - LiMn_{0.5}Ni_{0.5}O_2]$ [29]. This assumed composition is further supported by the electrochemical data presented later.

Concerning the films obtained from $Li_{1/2}MNO$ target, they present a structure similar to $Ni_{2/3}Mn_2O_4$ spinel in which Mn and Ni occupy both octahedral and tetrahedral sites [29], the position occupied by Li ions is, however, not revealed. In the case of this composition, it is probable that the concentration of Li is insufficient to displace all transition metal cations into octahedral sites as is normally the case in the LMNO spinel where Li occupies 1/8 of the tetrahedral sites and Mn and Ni occupy 1/2 of the octahedral sites.

The surface of the pristine electrodes was analyzed using XPS, Fig. 3. The C 1*s* signals mainly show aliphatic carbon (284.8 eV) with weak responses from species containing C–O and C=O bonds at 286 and 288.3 eV, respectively. These responses are also measured

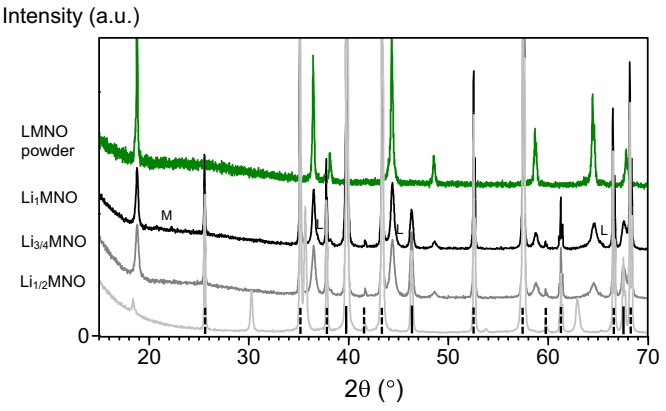

Fig. 2. XRD patterns of annealed LMNO films grown onto Al_2O_3/Pt substrates, respectively sputtered from stoichiometric (Li_1MNO) and Li deficient ($Li_{3/4}MNO$ and $Li_{1/2}MNO$) targets. A reference pattern for LMNO spinel powder is given as reference to ease the identification of the diffraction peaks. L and M denote layered $LiMn_{0.5}Ni_{0.5}O_2$ and monoclinic Li_2MnO_3 phases, respectively. Vertical dashed and full bars represent the diffraction lines for Al_2O_3 and Pt, respectively.

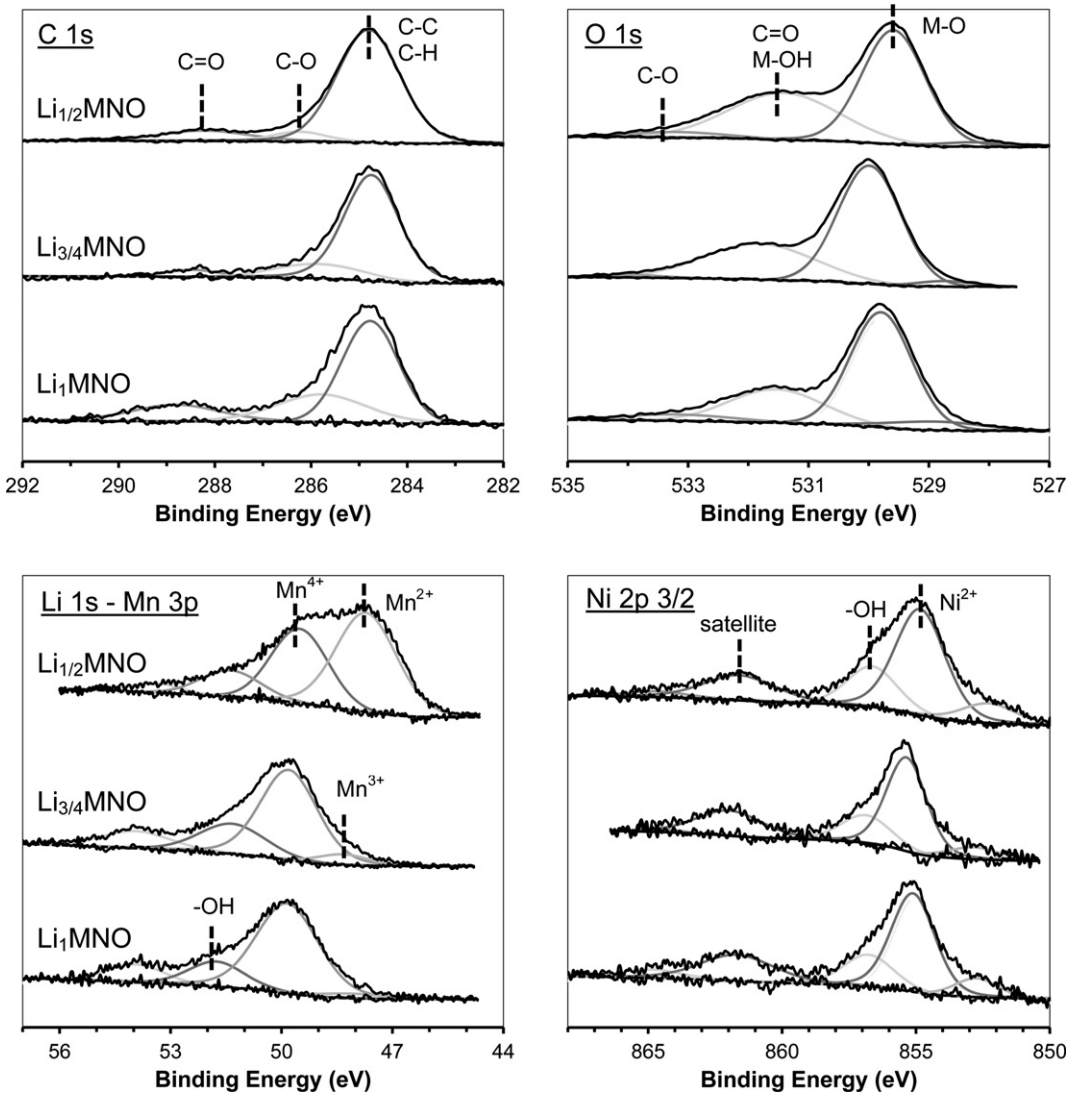

Fig. 3. Surface chemistry of pristine LMNO thin films measured by XPS. The C 1*s*, O 1*s*, Mn 3*p*, Li 1*s*, and Ni 2*p*3/2 regions are presented. The spectra are deconvoluted using Gaussian–Lorentzian functions. The background and residue functions are also shown.

on the O 1*s* binding level at energies of typically 531.5 and 533.5 eV. The response at 531.5 eV is, however, much larger than the response measured for carbon at 288.3 eV for C=O, which indicates that another O bond needs to be taken into account. Likely, −OH groups are also present on the surface, as will be discussed with the transition metals signals. The main peak in the O1*s* corresponds to oxygen atoms from the lattice and is found around 529.5–530 eV.

The Mn 3*p* and Ni 2*p* spectra clearly show similar responses for the films obtained from $Li_{3/4}MNO$ and Li_1MNO targets. The values of the peak energies for the Mn 3*p* and Ni 2*p*3/2 signals are reported in Table 3. Deconvolution of the core level 2*p*3/2 signal into three peaks lead to a major response in the center, at about 49.9 and 855.3 eV for the and Ni 2*p*3/2 signals, respectively. On the sides, weaker signals are visible at about 852.5–853 eV and 857 eV for Ni 2*p*3/2, and 48.3 and 51.5–52.0 eV for Mn 3*p*. The attribution of the spectra for Mn 3*p* and Ni 2*p* is done assuming that Mn are tetravalent ions whereas Ni are divalent ions. The surrounding peaks can be ascribed to Mn^{3+} at lower binding energies and hydroxyl groups (−OH) at higher energies. The weak signal measured at lower energy for Ni 2*p* is not completely understood. The Li 1s signal show a single peak around 54 eV, attributed to Li atoms from the LMNO structure.

For the films sputtered from $Li_{1/2}MNO$ target, the Li 1*s* signal decreases substantially and a strong signal is detected around 47.7 eV, attributed to Mn^{2+} ions from the $Ni_{2/3}Mn_2O_4$-type structure. Moreover, signal from Mn^{4+} is clearly visible around 49.6 eV. In $NiMn_2O_4$, Ni and Mn ideally have formal oxidation states of +2 and +3, respectively. However, it is documented that Mn^{3+} disproportionate into Mn^{2+} and Mn^{4+} in $NiMn_2O_4$ [33]. When the structure is Ni deficient, e.g. $Ni_{2/3}Mn_2O_4$ as here, the lower amount of Ni is compensated by further oxidation of Mn^{3+} in Mn^{4+}.

Table 3
Peak assignment from fitting the XPS high resolution scans measured on thin films. Energies in eV.

XPS signal	Li_1MNO	$Li_{3/4}MNO$	$Li_{1/2}MNO$	Assignment
Li 1*s*	54.05	54.03	53.41	Li
Mn 3*p*	/	/	47.67	Mn^{2+}
Mn 3*p*	48.27	48.46	48.46	Mn^{3+}
Mn 3*p*	49.99	49.86	49.57	Mn^{4+}
Mn 3*p*	51.90	51.44	51.39	−OH
Ni 2*p*3/2	852.90	852.92	852.49	?
Ni 2*p*3/2	855.26	855.38	854.99	Ni^{2+}
Ni 2*p*3/2	856.99	857.01	856.79	−OH

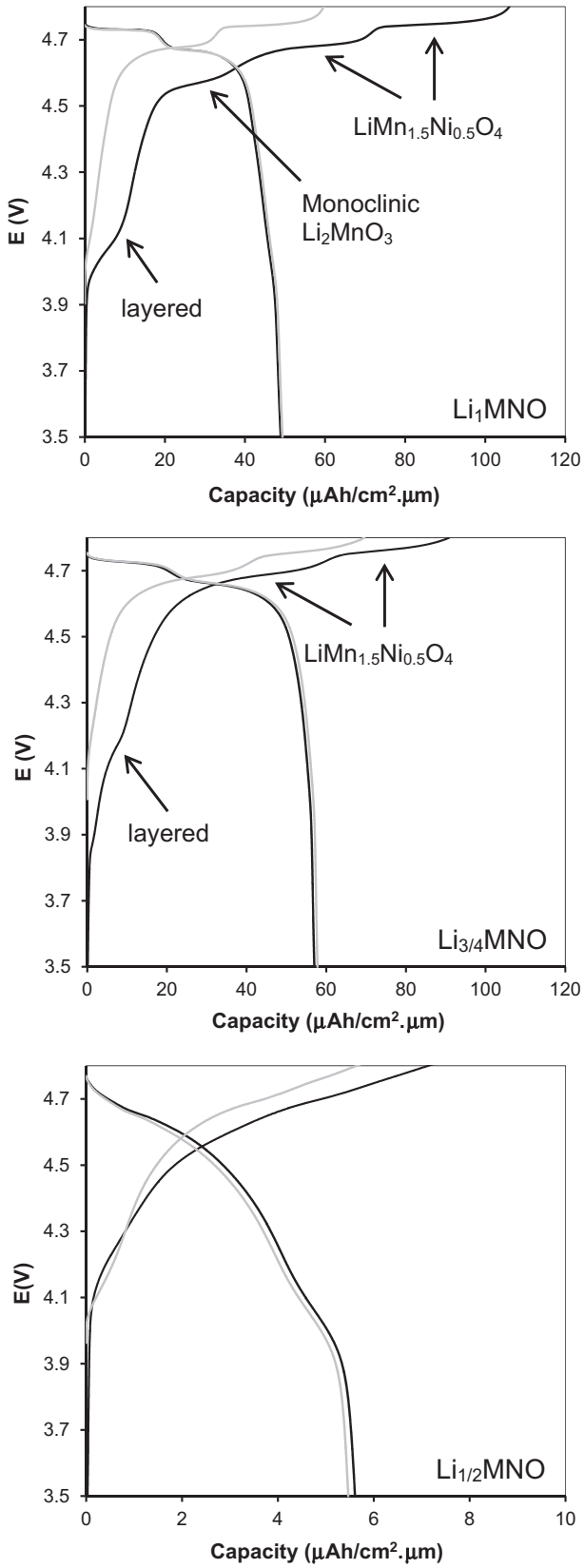

Fig. 4. Typical electrochemical potential profiles of LMNO thin films sputtered from Li_1MNO, $Li_{3/4}MNO$ and $Li_{1/2}MNO$ targets during the first (black) and second (grey) cycles.

Moreover, as Li enters the structure, further oxidation of Mn^{3+} is expected. All these expectations are well confirmed here with the Mn signal showing large amounts of Mn^{2+} and Mn^{4+}. Furthermore, the Ni 2*p* signal is similar to those measured for the other compositions, which further confirms the formation of a $Ni_{2/3}Mn_2O_4$ type structure in which Ni ions are divalent. Looking at the surface composition (c.f. Table 2), the surface seems to be depleted by Ni ions as the Li content decreases, whereas the Mn/Ni ratio in the bulk remains more or less the same.

The thin film cathodes have distinct electrochemical responses, as presented in Fig. 4. The formation of a layered-spinel thin film material is substantiated by the electrochemical potential profile of the films sputtered from Li_1MNO target. The first charge show characteristics of a layered phase such as $LiMn_{0.5}Ni_{0.5}O_2$ between 4 and 4.5 V and a distinctive plateau around 4.55 V which is normally attributed to the net loss of Li_2O from Li_2MnO_3 [28]. The rest of the charge displays the two well-known plateaus centered around 4.7 V resulting from the LMNO spinel phase. During the subsequent discharge, and the subsequent cycle, the reactions below 4.6 V are almost completely absent and only a weak inflexion around 4.0 V is visible. This reaction can probably be ascribed to the oxidation of Mn^{3+} into Mn^{4+} within the LMNO spinel, as is very well documented [2]. Therefore, the response between 4 and 4.5 V during the first charge can also account to a small extent for the oxidation of Mn^{3+} present inside the LMNO spinel.

In summary, the electrochemical reaction during the first charge is assumed to consist of the oxidation of Ni^{2+} into Ni^{3+} then Ni^{4+} within a layered phase of possible composition $LiMn_{0.5}Ni_{0.5}O_2$ (4–4.5 V), the decomposition of Li_2MnO_3 into MnO_2, O_2 gas and Li ions and electrons (4.5–4.6 V), and the oxidation of Ni^{2+} into Ni^{3+} then Ni^{4+} within the LMNO spinel (>4.6 V). During the subsequent discharge, and subsequent cycles, Mn^{3+} present within the LMNO spinel is active around 4.0 V, but most of the reaction occurs around 4.7 V within the spinel due to the oxidation of Ni. Using a cut-off potential of 3.5 V, the formed MnO_2 is not expected to be electrochemically active [28]. However, the layered phase should provide some capacity. Although there is a small inflexion around 4.0 V during discharge, the capacity spent in that region is much lower than the capacity obtained from the layered phase during the first charge. Therefore, we hypothesize that the absence of response from the layered phase is indicative of the conversion into an inactive phase upon Li removal.

The theoretical capacity for the stoichiometric LMNO spinel is 65.5 $\mu Ah\,cm^{-2}\,\mu m^{-1}$ assuming a gravimetric capacity of

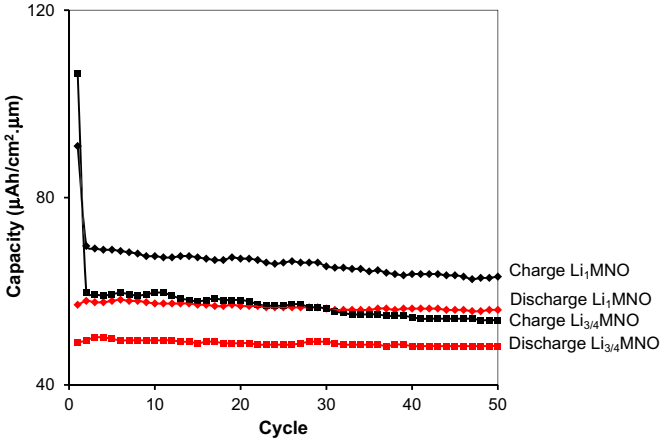

Fig. 5. Cycle life of LMNO thin films sputtered from Li_1MNO (square) and $Li_{3/4}MNO$ (diamonds) targets. Both charge (black) and discharge (red) capacity curves are presented. (For interpretation of the references to colour in this figure legend, the reader is referred to the web version of this article.)

146.7 mAh g^{-1} and 4.47 g cm^{-3} density. The initial charge capacity of these films is about 105 μAh cm^{-2} $μm^{-1}$ for a reversible capacity of about 50 μAh cm^{-2} $μm^{-1}$. The irreversible capacity during the first charge is related to the Li excess present as layered and Li_2MnO_3 materials as well as from the electrolyte decomposition. This is further evidenced during the second and subsequent cycles (not shown here) where the charge capacity remains high at about 60 μAh cm^{-2} $μm^{-1}$. A close comparison of the charge and discharge capacities spent in the 4–4.5, 4.5–4.6, 4.6–4.7 and 4.7–4.8 V indicates that the electrolyte decomposition is mostly taking place above 4.6 V, especially at potentials larger than 4.7 V.

For the films sputtered from a target of composition $Li_{3/4}MNO$, the response from a layered phase (4–4.5 V) is less pronounced while the plateau around 4.55 V attributed to the conversion of Li_2MnO_3 is absent. In addition, compared to the films sputtered from Li_1MNO target, the total charge capacity (about 90 μAh cm^{-2} $μm^{-1}$) is lower and the reversible capacity is higher (about 58 μAh cm^{-2} $μm^{-1}$). These results clearly indicate that the Li content in the films sputtered from an Li deficient target is lower, as expected, however it is still high enough to create a material which is close to being stoichiometric and have a capacity close to the theoretical value (about 65.5 μAh cm^{-2} $μm^{-1}$). During the subsequent cycle, the removal of Li ions mostly takes place around 4.7 V within the spinel as there is hardly any response observed below 4.6 V. The second charge capacity (about 68 μAh cm^{-2} $μm^{-1}$) is higher than the corresponding discharge capacity (58 μAh cm^{-2} μm), as also found for the films sputtered from Li_1MNO target, and is also attributed to the electrolyte continuous decomposition above 4.6 V.

The films obtained from a target of composition $Li_{1/2}MNO$ present a rather sloping potential profile response and much lower capacities. The redox couples involved in the different regions of the profiles are not clearly evidenced. The capacity from these films is much lower, as is expected from the lower Li 1*s* signal evidenced in XPS (Fig. 3). Nonetheless, the measured capacity is much lower than that expected for films sputtered from a target of composition

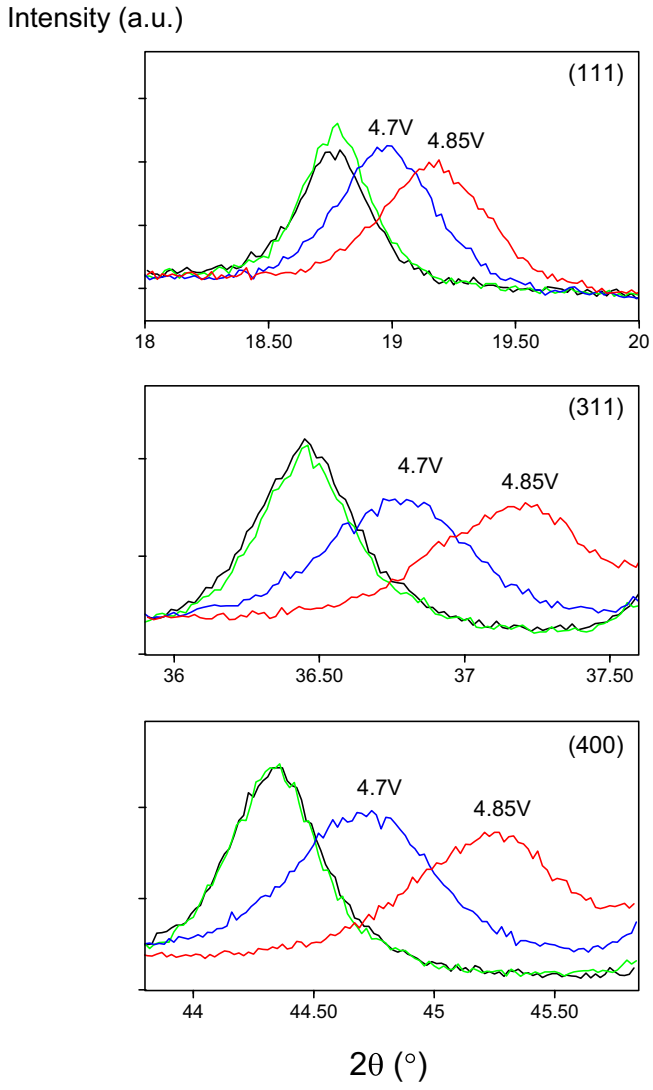

Fig. 6. Characterization of structural changes by XRD for LMNO thin films sputtered from $Li_{3/4}MNO$ target. XRD patterns for pristine (black), 4.7 V charged (blue), 4.85 V charged (red) and 1 time cycled at (3.5 V, green) electrodes are presented for the (111), (311) and (400) diffraction peaks. (For interpretation of the references to colour in this figure legend, the reader is referred to the web version of this article.)

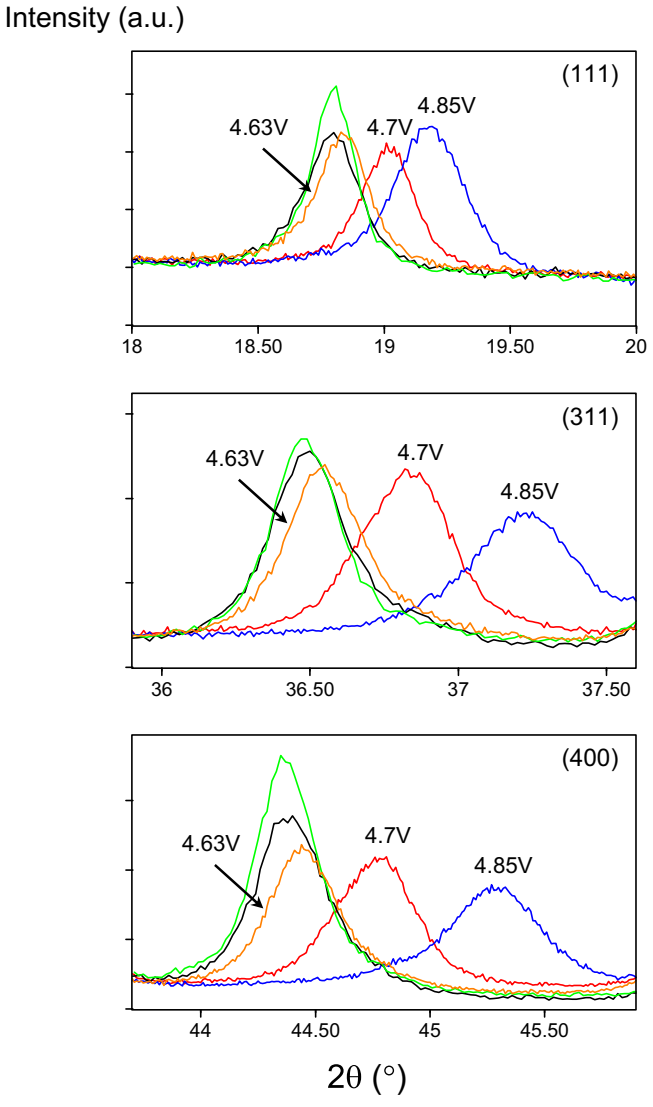

Fig. 7. Characterization of structural changes by XRD for LMNO thin films sputtered from Li_1MNO target during the first electrochemical cycle. XRD patterns for pristine (black), 4.63 V (orange), 4.7 V charged (red), 4.85 V charged (blue) and 1 time cycled (3.5 V, green) electrodes are presented for the (111), (311) and (400) diffraction peaks. (For interpretation of the references to colour in this figure legend, the reader is referred to the web version of this article.)

Table 4
Lattice parameters (nm) obtained from Rietveld refinements for LMNO films sputtered from $Li_{3/4}MNO$ and Li_1MNO targets and cycled to various potentials.

Target	As-prepared	4.63 V	4.7 V	4.85 V	1 Cycle (3.5 V)
$Li_{3/4}MNO$	0.8164	/	0.8104	0.8015	0.8166
Li_1MNO	0.8161	0.8151	0.8107	0.8011	0.8163

$Li_{0.5}MNO$. The reasons for the apparent trapping of Li ions inside this spinel structure isostructural to $Ni_{2/3}Mn_2O_4$ are not understood at this moment and may perhaps result from the presence of Mn^{2+} in the structure.

The cycle life of these films is presented in Fig. 5. Over 50 cycles, the cycle life is good and the change in composition does not drastically affect the material capacity retention. As previously discussed, the capacity of films sputtered from $Li_{3/4}MNO$ is somewhat higher than that of films sputtered from Li_1MNO. In both cases, the initial irreversible capacity is high and does not decrease to zero during the subsequent cycles, which we attribute to the electrolyte continuous decomposition at high voltages, resulting in the formation of a CEI. Nonetheless, the good capacity retention over many cycles ensure that these sputtered films are very good candidates for studying the material intrinsic properties.

The change in crystallographic structure of the films produced from $Li_{3/4}MNO$ and Li_1MNO targets were characterized using XRD on thick films, Figs. 6 and 7, respectively. The regions for the most intense peaks are presented. In the case of films sputtered from $Li_{3/4}MNO$ target, the peaks have shifted to higher angles as Li is removed from the electrode, which indicates a decrease of the lattice parameter of the cubic spinel phase. Upon completion of one cycle, at full discharge at 3.5 V, the peak position is very close to that of the starting material, which indicates that the cycled structure recovers its original size. Rietveld refinements of these patterns were performed, and the resulting lattice parameters assuming a spinel phase of group symmetry Fd-3m are presented in Table 4. The lattice parameter of the starting structure (0.8164 nm) is close to that expected for the cation ordered LMNO spinel phase (0.8167 nm, space group $P4_332$) in which Ni occupies the 4a sites and Mn the 12b sites [34]. This is further correlated by the lattice parameter obtained at half-charge (4.7 V, 0.8104 nm) and full charge (4.85 V, 0.8015 nm), in good agreement with *in situ* XRD results by Kunduraci et al. [34]. The voltage separation between the two plateaus is, however, larger than that observed for the ordered spinel. It is here typically 60 mV as opposed to about 20 mV for the transition metal ordered $P4_332$ spinel [34]. The reason for this apparent contradiction is not clear and beyond the current scope.

In the case of the films obtained from Li_1MNO target, the changes in structure are comparable based on the change of the peak position upon cycling (Fig. 7), and the lattice parameter evolution (Table 4) is comparable with reported values [32] and to those found for the films obtained from $Li_{3/4}MNO$ target. Interestingly, the electrode charged at 4.63 V has only a slight shift of the peak position corresponding to a lattice parameter decrease to 0.8151 nm. From the potential profile (Fig. 4, upper plot) it is clear that a substantial amount of Li ions has been extracted at 4.63 V. We initially selected this potential as the point where the spinel would not have released Li ions at all, which appeared to be slightly too high. Nonetheless, it is evident that the reaction of the spinel phase has just started at 4.63 V given the small reduction in lattice parameter. Assuming a linear relationship between lattice parameter and Li content, this decrease in lattice parameter corresponds to about 7% of Li removed from the spinel phase, which suggests that Li ions extracted below 4.6 V are resulting from a different phase than the spinel phase. The weak diffraction peaks between 21 and 23° seem to have disappeared upon charging, however this is questionable given their initial weak intensity (Fig. 2). The

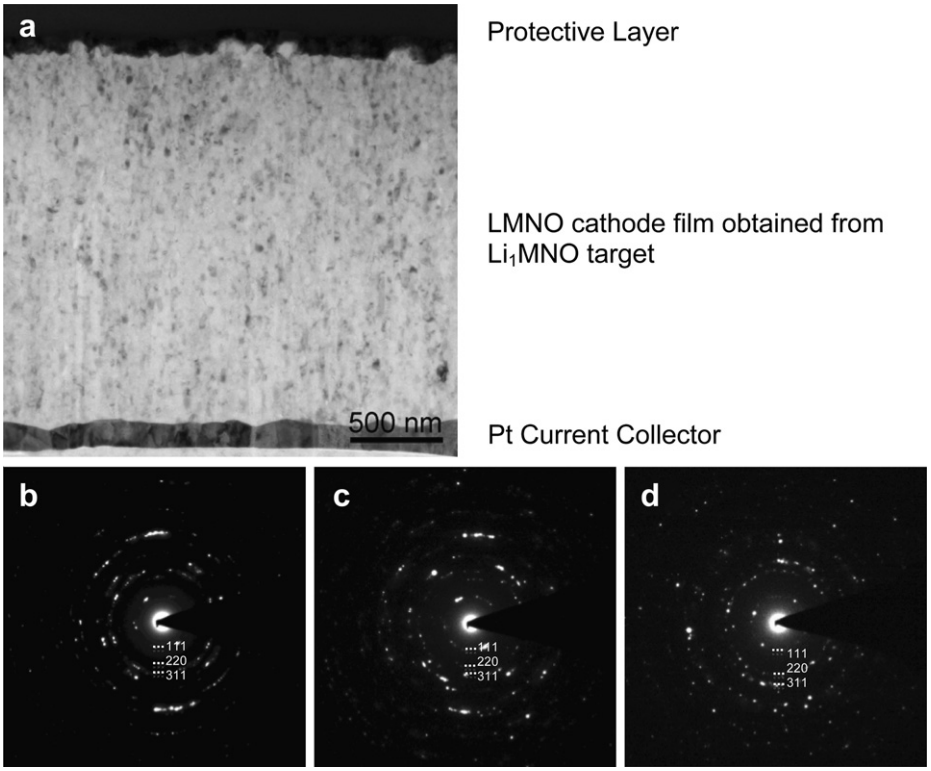

Fig. 8. (a) Bright-field TEM micrograph of an electrochemically cycled LMNO cathode film obtained from Li_1MNO target. SAED patterns corresponding to (b) charge at 4.63 V, (c) charge at 4.75 V and (d) full charge–discharge cycle (4.8–3.5 V).

intensities of the peaks denoted by *L* in Fig. 2 for a layered phase are also very weak and do not allow a clear discussion on the presence and transformation of a layered phase.

In order to understand the change in structure at the nanoscale, we investigated this electrode material at various voltages using TEM. The structural evolution was measured for the samples charged at the start of the first plateau (4.63 V), during the second plateau (4.75 V) and after a full charge-discharge cycle (4.8–3.5 V). Fig. 8a shows a representative bright-field TEM image from an FIB-prepared TEM cross-section. SAED was used to determine the crystal structure of the cathode materials and to correlate with structural information gained from XRD. The ED ring patterns (Fig. 8b–d) were measured and indexed for all three specimens and the results show similar reflections, which can all be assigned to the LMNO spinel phase. Due to the size scale of the selected area aperture used for electron diffraction experiments, the ED patterns were acquired only from a small fraction of grains from the thin film cathode material. Therefore, it was not possible to discern possible differences between individual layered and spinel phases and respective fractions thereof. Hence, HRTEM was used to determine

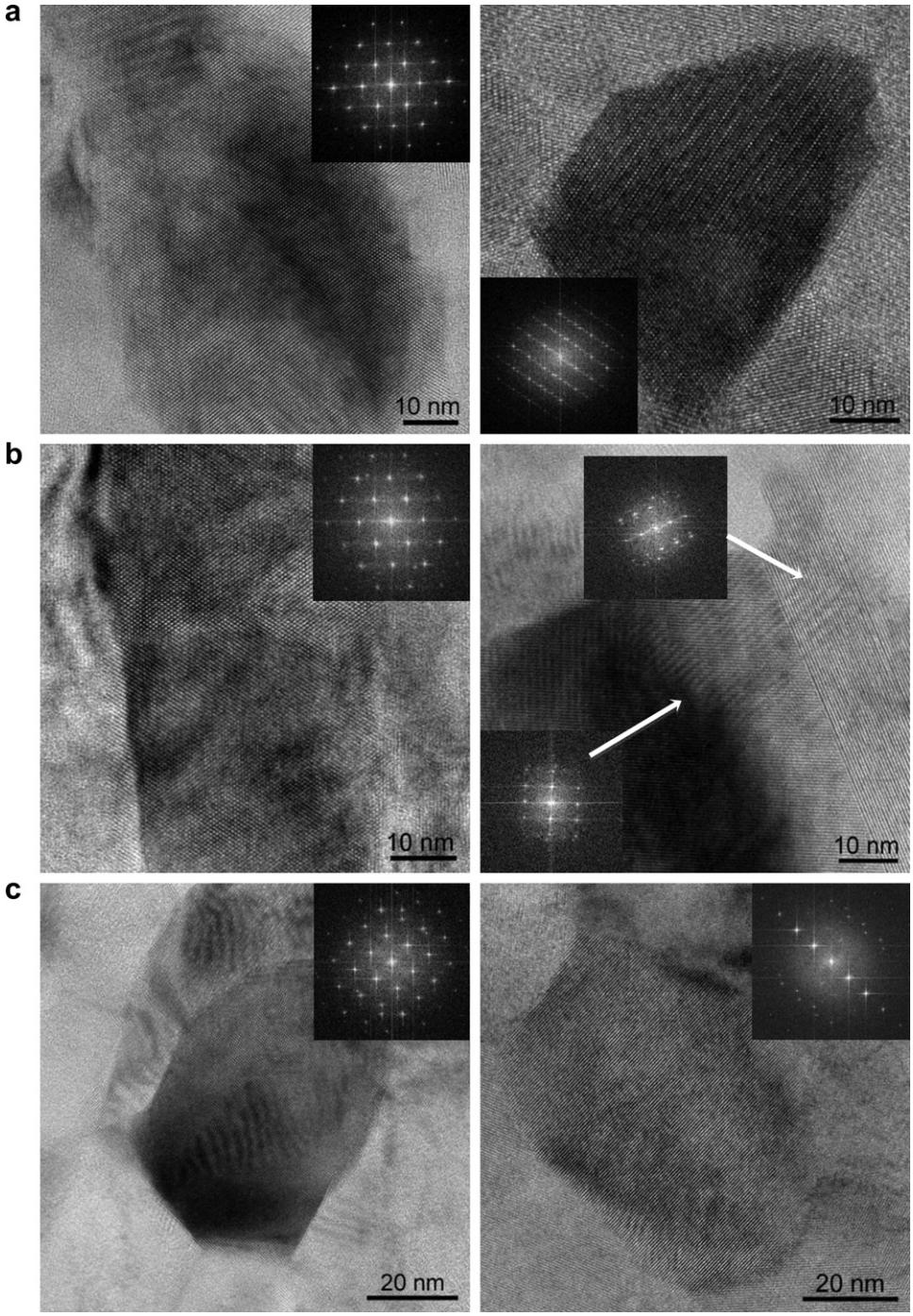

Fig. 9. HRTEM images from FIB-prepared TEM cross-sections of electrochemically cycled LMNO cathode films obtained from Li_1MNO target following (a) charge to 4.63 V, (b) charge to 4.75 V and (c) full charge-discharge cycle (4.8–3.5 V).

the structure of individual grains through measurements of lattice spacing from Fast Fourier Transforms (FFT) of the HRTEM lattices fringes (Fig. 9a–c). The first images in each set clearly show grains that are oriented along the [110] zone axis with lattice reflections corresponding the LMNO spinel phase. Additional HRTEM images from the respective conditions represent examples of grains possessing phases that could not be identified through lattice spacing measurements or correlated with LMNO-layered, LMNO spinel, Li_2MnO_3, $LiMn_2O_4$, or $LiMnO_2$. Further detailed analysis of possible phase transformations are being conducted.

EELS was employed to monitor the changes in oxidation state of the transition metals, especially Ni, on these (dis)charged thin film cathodes. Although the white line intensity ratio (WLR) found for Mn was found to be nearly constant for all samples, the variation of the Ni WLR did not clearly evidence an oxidation of Ni upon charging (see Supplementary Information). However, it is clear from the XRD results that the lattice shrinks accordingly to the expected mechanism in which Ni^{2+} is oxidized. We therefore suspect that the thinning of the thin film samples by means of FIB using high energy Ga ions (40 kV), as is commonly performed, detrimentally modifies the transition metal oxidation states.

The rate capability of (un)coated LMNO thin films obtained from Li_1MNO target is presented in Fig. 10. It is clear that the bare material measured in a liquid electrolyte have a high rate capability as it can retain about 85% of the reversible capacity at 100 C-rate. This value is in fact an underestimate of the material intrinsic performance. Indeed, the two-electrode cell configuration also includes the overpotential contributions from the Li counter electrode, which may become significant for high currents. When the electrode is covered by a thin layer of ZnO, the rate performance decreases as only about 70% of the capacity can be recovered at 100 C-rate. Still the rate performance remains high. More importantly, it is clear that covering the electrode with a thin layer of ZnO decreases the irreversible capacity. Further decrease in the irreversible capacity is obtained when the electrode is covered by an electronically insulating but ionically conductive material, i.e. LiPON, of somewhat larger thickness. This indicates that preventing electron transfer to occur directly on the cathode surface but at the electrode/LiPON interface is essential for reducing coulombic losses resulting from the electrolyte decomposition (CEI formation). The rate capability of LiPON-coated electrodes is, however, substantially decreased as only about 40% of the reversible capacity can be extracted at 100 C-rate. Nonetheless, the overall rate capability of these sputter deposited films remains high compared to uncoated LMNO thin film systems prepared by others [21–25].

In short, the rate capability of these LMNO thin films is very high. Moreover, coating the electrode surface decreases the irreversible capacity but at the cost of some rate performance. The reasons for the poorer rate performance are likely due to changes in surface kinetics. Instead of a transfer from solvated Li ions from the liquid electrolyte onto the electrode surface and subsequent reaction, the transfer now takes onto ZnO or LiPON. In addition, ionic conduction through the coating is necessary for Li ions to reach the LMNO electrode surface. There is also an additional transfer resistance at the coating/electrode interface. Coating with a thick layer (here LiPON) may also reduce the electrode surface area, thus decreasing the contact area with the electrolyte solution.

In order to evaluate more quantitatively the additional impedance resulting from the coating, EIS was performed at various potentials during discharge, as shown in Fig. 11. For the bare electrode measured in the liquid electrolyte, the impedance is composed of suppressed semi-circles and a straight line at lower frequencies. The former is related to the charge transfer at the cathode and Li counter electrode interfaces whereas the latter is representative of the semi-infinite diffusion of Li ions within the cathode and electrolyte. The width of the semi-circle decreases from 4.9 to 4.75 V and increases as the potential decreases from 4.75 to 3.7 V. The minimum value for the semi-circle width is around 170 Ω for 4.725 or 4.75 V.

When the electrode is covered by a thin layer of ZnO, the variation of the semi-circle width remains the same. However, the semi-circles become even more suppressed and the overall width

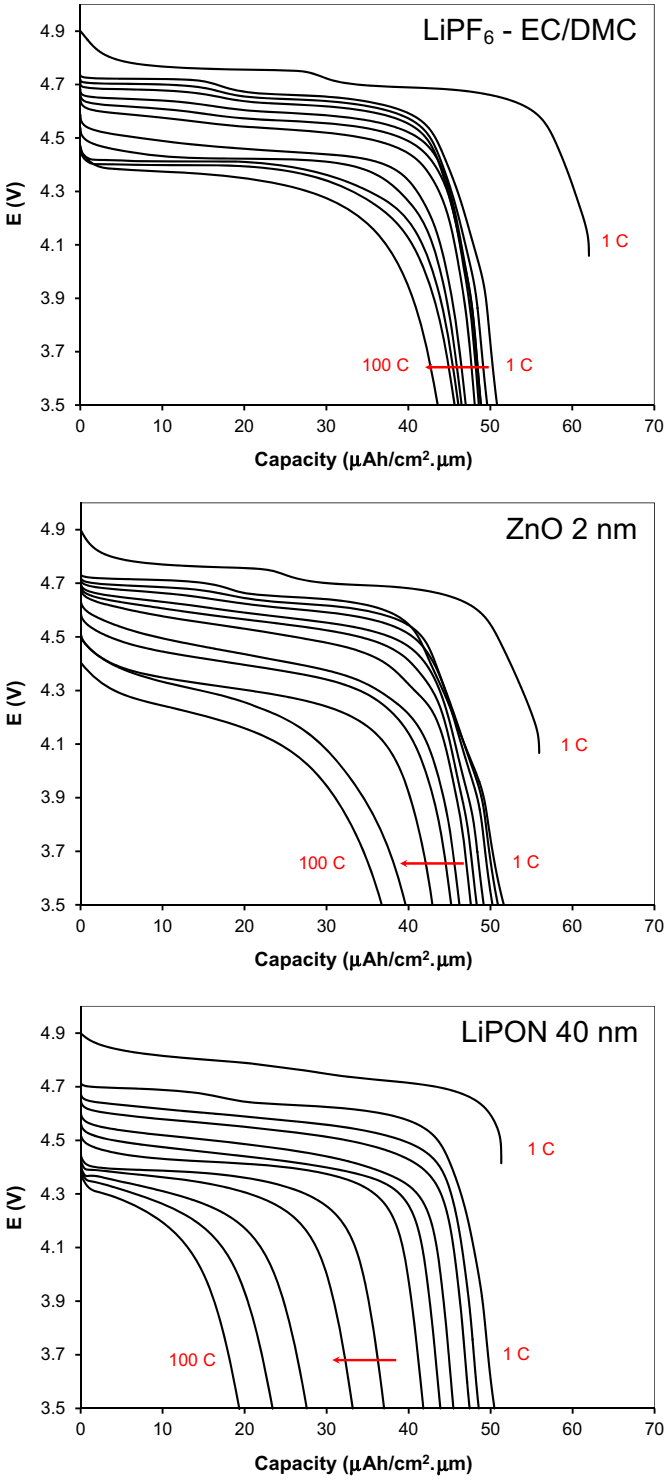

Fig. 10. Discharge rate capability of bare, ZnO coated and LiPON-coated LMNO thin film electrodes (Li_1MNO target, 0.4 μm thick) measured in 1.2 M $LiPF_6$ in EC/DMC. The cells were charged at 1C-rate and discharged from 1 to 100 C-rate.

increases from a minimum of about 250 Ω for 4.725 or 4.75 V. This increase in impedance can be related to the additional resistances resulting from the coating at both electrode and electrolyte interfaces, and due to the ionic conduction through the layer. When a LiPON film of 40 nm is present on the electrode surface, the variation of the semi-circle width also remains the same. However, the semi-circle width increases by several folds with a minimum value of about 1000 Ω at 4.725 or 4.75 V. Although the internal processes responsible for the increase in impedance cannot be ascribed unambiguously, it is clear that covering LMNO thin film electrode with a coating increases the impedance of the electrode. Moreover, these results obviously corroborates the rate performance results shown in Fig. 10, which indicated poorer performance for ZnO-covered electrodes, and even poorer for electrodes covered by a thicker coating of LiPON. Nonetheless, it should be reminded that the rate performance of these coated LMNO thin film cathodes remains very high and is higher than those of bare and thinner LMNO films obtained by ESD or PLD [21–24].

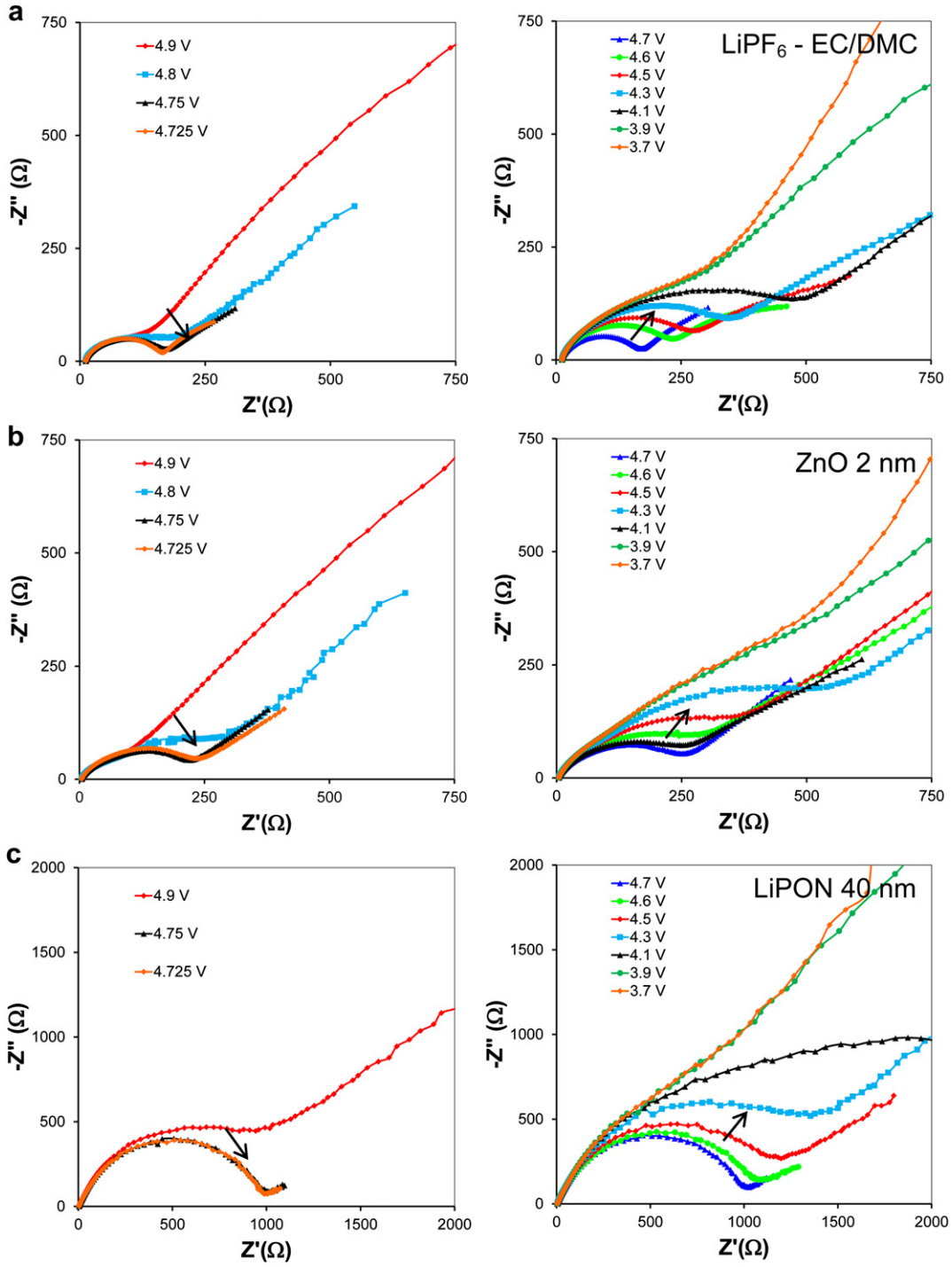

Fig. 11. Impedance Nyquist plots during discharging (a) bare, (b) ZnO coated and (c) LiPON-coated LMNO thin film electrodes (Li_1MNO target, 0.4 μm thick). Cells were cycled 10 times before impedance was measured. Impedance was recorded after a potentiostatic discharge of 1 h at each voltage.

4. Conclusions

Lithium manganese nickel oxide thin films have been prepared by means of magnetron sputtering from homemade targets of varying Li contents. Sputtering from a stoichiometric LMNO target (Li/Mn = 2/3) results in the formation of Li-rich films composed of a mixture of spinel, layered and monoclinic phases, similarly to layered-spinel composite electrodes. The layered and monoclinic phases convert during the first electrochemical charge into inactive compounds whereas the spinel phase remains active at 4.7 V. Films obtained from a Li deficient target (Li/Mn = 1/2) are mostly composed of a spinel phase along with a minor layered phase. Sputtering from a target with a further lower Li content (Li/Mn = 1/3) results in the formation of a spinel phase isostructural to $Ni_{2/3}Mn_2O_4$ with a much lower storage capacity for Li ions. The capacity retention of these films is good and the rate performance is very high with typically 85% of delivered capacity at 100 C-rate.

The role of coating these high voltage cathodes was also explored using ZnO and LiPON thin films. The rate performance of coated electrodes was found to be poorer, as expected and confirmed by EIS. Nonetheless, the rate performance of these (un) coated sputtered films is much higher than bare LMNO thin films system prepared by other methods (ESD or PLD). We also found out that coating the electrode reduces the coulombic losses inherent to the high voltage cathode measured in liquid electrolyte, although it cannot completely suppress it. Current efforts are now being devoted to understanding the surface chemistry of coated thin film high voltage cathodes.

Acknowledgements

This research was supported by the Laboratory Directed Research and Development Program of Oak Ridge National Laboratory, managed by UT-Battelle, LLC, for the U.S. Department of Energy. Microscopy research was also supported by ORNL SHaRE user facility, which is sponsored by the Scientific User Facilities Division, Office of Basic Energy Sciences, U.S. Department of Energy.

Appendix A. Supplementary data

Supplementary data related to this article can be found online at doi:10.1016/j.jpowsour.2012.03.076.

References

[1] M. Armand, J.M. Tarascon, Nature 451 (2008) 652–657.
[2] R. Santhanam, B. Rambabu, J. Power Sources 195 (2010) 5442–5451.
[3] Q. Zhong, A. Bonakdarpour, M. Zhang, Y. Gao, J.R. Dahn, J. Electrochem. Soc. 144 (1997) 205–213.
[4] Y. Gao, K. Myrtle, M. Zhang, J.N. Reimers, J.R. Dahn, Phys. Rev. B 54 (1996) 16,670–16,675.
[5] K.M. Shaju, P.G. Bruce, Dalton Trans. (2008) 5471–5475.
[6] X. Ma, B. Kang, G. Ceder, J. Electrochem. Soc. 157 (2010) A925–A931.
[7] M. Kunduraci, J.F. Al-Sharab, G.G. Amatucci, Chem. Mater. 18 (2006) 3585–3592.
[8] S. Patoux, L. Sannier, H. Lignier, Y. Reynier, C. Bourbon, S. Jouanneau, F. Le Cras, S. Martinet, Electrochim. Acta 53 (2008) 4137–4145.
[9] Z. Chen, Y. Qin, K. Amine, Y.-K. Sun, J Mater Chem 20 (2010) 7606–7612.
[10] S. Patoux, L. Daniel, C. Bourbon, H. Lignier, C. Pagano, F. Le Cras, S. Jouanneau, S. Martinet, J. Power Sources 189 (2009) 344–352.
[11] H. Duncan, D. Duguay, Y. Abu-Lebdeh, I.J. Davidson, J. Electrochem. Soc. 158 (2011) A537–A545.
[12] Y.-K. Sun, K.-J. Hong, J. Prakash, K. Amine, Electrochem. Commun. 4 (2002) 344–348.
[13] Y. Kobayashi, H. Miyashiro, K. Takei, H. Shigemura, M. Tabuchi, H. Kageyama, T. Iwahori, J. Electrochem. Soc. 150 (2003) A1577–A1582.
[14] Y.-K. Sun, C.S. Yoon, I.-H. Oh, Electrochim. Acta 48 (2003) 503–506.
[15] J. Arrebola, A. Caballero, L. Hernán, J. Morales, E. Rodríguez Castellón, J.R. Ramos Barrado, J. Electrochem. Soc. 154 (2007) A178–A184.
[16] Y. Fab, J. Wang, Z. Tang, W. He, J. Zhang, Electrochim. Acta 52 (2007) 3870–3875.
[17] T. Noguchi, I. Yamazaki, T. Numata, M. Shirakata, J. Power Sources 174 (2007) 359–365.
[18] H.-B. Kang, S.-T. Myung, K. Amine, S.-M. Lee, Y.-K. Sun, J. Power Sources 195 (2010) 2023–2028.
[19] H.M. Wu, I. Belharouak, A. Abouimrane, Y.-K. Sun, K. Amine, J. Power Sources 195 (2010) 2909–2913.
[20] J.Y. Shi, C.-W. Yi, K. Kim, J. Power Sources 195 (2010) 6860–6866.
[21] M. Mohamedi, M. Makino, K. Dokko, T. Itoh, I. Uchida, Electrochim. Acta 48 (2002) 79–84.
[22] K. Dokko, M. Mohamedi, N. Anzue, T. Itoh, I. Uchida, J. Mater. Chem. 12 (2002) 3688–3693.
[23] H. Xia, S.B. Tang, L. Lu, Y.S. Meng, G. Ceder, Electrochim. Acta 52 (2007) 2822–2828.
[24] H. Xia, Y.S. Meng, L. Lu, G. Ceder, J. Electrochem. Soc. 154 (2007) A737–A743.
[25] J.C. Arrebola, A. Caballero, L. Hernán, M. Melero, J. Morales, E.R. Castellón, J. Power Sources 162 (2006) 606–613.
[26] N.J. Dudney, J.B. Bates, R.A. Zuhr, S. Young, J.D. Robertson, H.P. Jun, S.A. Hackney, J. Electrochem. Soc. 146 (1999) 2455–2464.
[27] J.B. Bates, N.J. Dudney, B. Neudecker, A. Ueda, C.D. Evans, Solid State Ionics 135 (2000) 33–45.
[28] S.-H. Park, S.-H. Kang, C.S. Johnson, K. Amine, M.M. Thackeray, Electrochem. Commun. 9 (2007) 262–268.
[29] J. Cabana, S.-H. Kang, C.S. Johnson, M.M. Thackeray, C.P. Grey, J. Electrochem. Soc. 156 (2009) A730–A736.
[30] L. Baggetto, R.A.H. Niessen, F. Roozeboom, P.H.L. Notten, Adv. Funct. Mater 18 (2008) 1057–1066.
[31] J.F.M. Oudenhoven, T. van Dongen, R.A.H. Niessen, M.H.J.M. de Croon, P.H.L. Notten, J. Electrochem. Soc. 156 (2009) D169–D174.
[32] N.M. Hagh, G.G. Amatucci, J. Power Sources 195 (2010) 5005–5012.
[33] J. Töpfer, A. Feltz, D. Gräf, B. Hackl, L. Raupach, P. Weissbrodt, Phys. Stat. A 134 (1992) 405–415.
[34] M. Kunduraci, G.G. Amatucci, J. Electrochem. Soc. 153 (2006) A1345–A1352.